THE JOURNAL OF
PHYSICAL CHEMISTRY C

Article

pubs.acs.org/JPCC

Small Particles of Chemically-Reduced Graphene with Improved Electrochemical Capacity

Qing-Qiang Kong,[†] Cheng-Meng Chen,*[,†] Qiang Zhang,[‡] Xing-Hua Zhang,[†] Mao-Zhang Wang,[†] and Rong Cai[†]

[†]Key Laboratory of Carbon Materials, Institute of Coal Chemistry, Chinese Academy of Sciences, 27 Taoyuan South Road, Taiyuan 030001, China

[‡]Beijing Key Laboratory of Green Chemical Reaction Engineering and Technology, Department of Chemical Engineering, Tsinghua University, Beijing 10084, China

Supporting Information

ABSTRACT: Chemically reduced graphenes (CRGs) of different sizes were prepared by the reduction of graphene oxide (GO) in different oxidation degrees, with hydrazine hydrate as the reducing agent. Compared with normally oxidized GO (46.9 wt %), the deeply oxidized GO particles have a higher oxygen content (50.4 wt %). The oxygen content of resulting CRG is correspondingly increased from 11.3 wt % of normal-sized CRG to 16.3 wt % of small-sized CRG, with a dramatic increase in specific surface area from 468.2 to 716.3 m^2/g. More graphene edges, which were highly decorated by pseudocapacitive-active sites, were exposed in the small-sized CRG. As a result, small-sized CRG has a much higher specific capacitance (192.1 F/g) than that of normal-sized CRG (132.3 F/g), which is attribute to the contribution of both electrochemical double layer capacitance by an increased surface area and pseudocapacitance by extra surface functional groups.

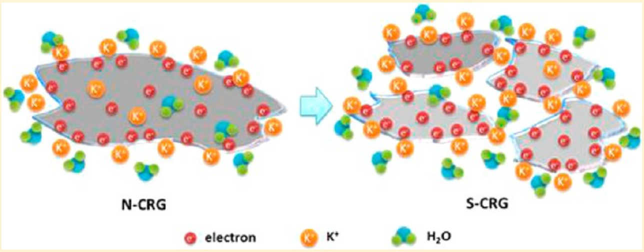

1. INTRODUCTION

Supercapacitors, also known as ultracapacitors or electrochemical capacitors, store charges at the electrode/electrolyte interface.[1,2] Compared with batteries, it is able to store and deliver energy in relatively shorter time with a higher power density (10 kW/kg). Meanwhile, the cycle life is up to a million cycles, which is several orders of magnitude higher than that of batteries.[3] These features have generated great interest in the applications of supercapacitors that include consumer electronics, hybrid electric vehicle, industrial power management, and so on.[4]

Carbon is one of the most widely used electrode materials for supercapacitors. It contributes to the electrochemical double layer capacitance (EDLC) by storing energy in the same way as a traditional capacitor and pseudocapacitance (PC) by a reversible electrochemical charge-transfer process at the same time.

Among all kinds of carbon materials, as a one-atom-thick crystal of sp^2 hybridized carbon, graphene with unique two-dimensional structure, high electronic conductivity, huge specific surface area, and excellent chemical stability has attracted great interest toward applications in energy storage such as supercapacitors and Li ion batteries.[5,6] Several investigations have reported the performance of graphene-based supercapacitors,[7] the specific capacitance of which can reach ~100 and 82 F/g in aqueous and organic electrolyte, respectively.[8] A large number of contributions have been devoted to improve the property of graphene-based supercapacitors, leading to improved specific capacitance values of 200, 120, and 75 F/g in aqueous, organic, and ionic liquid electrolyte, respectively.[9−11] In addition, three-dimensional hierarchically ordered porous graphene and hybridization of graphene and metal oxide or conducting polymers were explored to fully demonstrate the potentials of graphene-based supercapacitors.[12−17]

The ultimate performance of graphene-based electrodes is closely related to the microtexture, pore structure, and surface chemistry of graphene.[18−22] The lateral size is a key factor for applications in electrochemical energy storage, as the edges of a graphene sheet (mainly decorated by functional groups and dangling bonds) are believed to be more active than the sp^2-hybridized basal planes in the solution-based electrochemical process. With the longer oxidation time for graphene oxide (GO) preparation, the mean size of chemically reduced graphene (CRG) nanosheets decreased.[23,24] The investigation on the relevance between size-involved structural differences and the electrochemical performance is essential for the development of graphene-based energy storage devices. It will provide a new concept on materials chemistry of graphene, cast light on other electrochemistry properties, and also benefit further applications toward energy and sustainability.

Received: April 9, 2013
Revised: July 7, 2013
Published: July 8, 2013

In this contribution, the CRGs with different lateral sizes were prepared by reduction of GO at different oxidation degrees using hydrazine hydrate. The differences in microtexture, pore structure, surface chemistry, as well as the relevance between them and the electrochemical performance were systematically investigated.

2. EXPERIMENTAL SECTION

2.1. Preparation of CRG. Normal-sized GO (N-GO) was prepared by a modified Hummers' method, while small-sized GO (S-GO) was prepared by an improved approach, with a remarkably prolonged oxidation time from 1 to 72 h.[24,25] The CRG was prepared from the chemical reduction of as-prepared GO by hydrazine hydrate,[26] and the as-obtained products are denoted as N-CRG and S-CRG, respectively. More details can be found in the Supporting Information.

To identify the relative ratio of contribution from EDLC and PC to the electrode, the surface functionalities of N-CRG and S-CRG are further removed by annealing at 1000 °C in high vacuum for 15 min. The as-obtained control samples are denoted as N-CRG-H and S-CRG-H, respectively.

2.2. Characterizations. The morphologies of GO and CRG samples were characterized by atomic force microscope (AFM, Tip mode, Veeco NanoScope IIIa Mutimode, DI, USA), a JEOL JSM 7401F scanning electron microscope (SEM) operated at 3.0 kV, and a JEOL JEM 2010 transmission electron microscope (TEM) operated at 200 kV. The samples were ultrasonically dispersed in ethanol, and then a drop of the solution was deposited on a Lacey carbon film grid for TEM characterization. X-ray diffractions (XRD) were performed at room temperature (Cu Kα radiation, λ = 0.15406 nm, D8 Advance, BRUKER/AXS, Germany). Laser Raman spectroscopy was performed on power samples by using a Horiba Jobin Yvon LabRAM HR800 Raman spectrometer with a He−Ne laser excitated at 633 nm. The isotherm of N_2 physisorption was obtained at 77 K with use of a Micromeritics ASAP2020 V3.05 Brunauer−Emmett−Teller apparatus. The elemental analysis was conducted with a Vario ELcube elemental analyzer. The Fourier transform infrared spectroscopy (FTIR) was done on an EQUINOX 55 and the sample was prepressed with KBr into pellets before testing. X-ray photoelectron spectroscopy (XPS) was performed on the thermo VG ESCALAB 250 surface analysis system with the following parameters: Al Kα = 1486.6 eV, power = 150 W (HV=15 kV and I = 10 mA), spot size = 500 μm, pass energy 50.0 eV, and energy step size 0.1 eV. The X-ray photoelectron spectra were calibrated for both beam intensity and charging (reference the banding energy at 284.4 eV of C1s peak). Prior to fitting, a Shirley background was subtracted. Peak areas were normalized with theoretical cross sections to obtain the relative surface elemental compositions. The as-prepared GO samples were further characterized by a NETZSCH5 thermal gravimetric analysis (TGA) system in Ar atmosphere.

2.3. Electrochemical Measurements. The electrochemical performance of the as-obtained CRG was measured with a three-electrode system in 6.0 M KOH aqueous electrolyte at ambient temperature. Ni foam coated with electrode materials served as the working electrode, while a saturated calomel electrode and Pt slice served as the reference electrode and counter electrode, respectively. The electrode materials for the working electrode were prepared by mixing the CRG and poly(tetrafluoroethylene) with a weight ratio of 85:15. Each electrode was quantified to contain about 8.0 mg of active materials. Cyclic voltammetry (CV) curves (scan rates at 1, 3, 10, 50, 100, and 200 mV s^{-1}), Galvanostatic charging/discharging (GC) curves (current density under 0.5, 1, 5, 10, and 20 A g^{-1}), and electrochemical impedance spectroscopy (EIS) profiles (frequency from 200 kHz to 10 mHz) were performed with a CHI 760D electrochemical workstation.

3. RESULTS AND DISCUSSION

3.1. Characterization of GO and CRG. The GO with different oxidation degrees were prepared by a modified Hummers method. As shown in Figure 1a,b, the size of N-GO is ca. 1−2 μm while that of S-GO, which was over oxidized, is around 50−200 nm. The smaller GO particles introduce more active sites including lattice defects, dangling bonds, and oxygenic functional groups. The thickness of N-GO and S-GO is 1.34 and 1.03 nm (Figure 1c,d), respectively. These values are somewhat larger than the interlayer space (0.776 nm) of the GO due to the abundant functional groups on both sides of the graphene sheets which break the original sp^2 carbon conjugation and result in skeleton distortions of the graphene.[27−29] There are some wrinkles and fluctuations on the surface of graphene to maintain its stability at ambient temperature by decreasing the surface energy.[30]

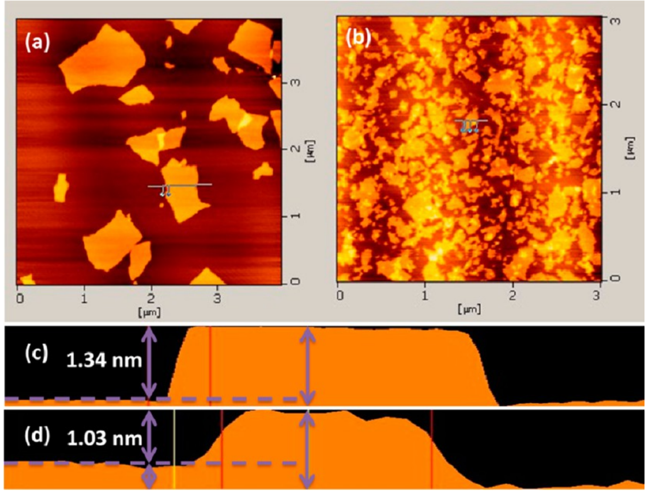

Figure 1. AFM images for (a) N-GO of overlook, (b) S-GO of overlook, (c) N-GO of lateral view, and (d) S-GO of lateral view.

The microstructure of the resulting CRG particles was characterized by SEM and TEM. As shown in Figure 2, both N-CRG and S-CRG exhibit typical disorder morphology of aggregated graphene, with mesopores distributed among the lateral edges of these wrinkled nanosheets. Compared with N-CRG (Figure 2a), S-CRG (Figure 2b) shows a much more compact structure that is attributed from the random assembly of smaller graphene sheets as unit building blocks. The TEM images (Figure 2c,d) indicate the typical waving and curving 2D structures of well-exfoliated graphene for N-CRG and S-CRG. However, S-CRG (Figure 2e,f) owns much more wrinkles with smaller scale in size than N-CRG (Figure 2c,d), which is attributable to the cracking of graphene during the over-oxidation process.

XRD, Raman spectroscopy, as well as N_2 adsorption were employed to investigate the structural difference between the two kinds of GO and CRG. As shown in Figure 3a, the interlayer space ($d_{(002)}$) of S-GO (0.781 nm) is relatively larger

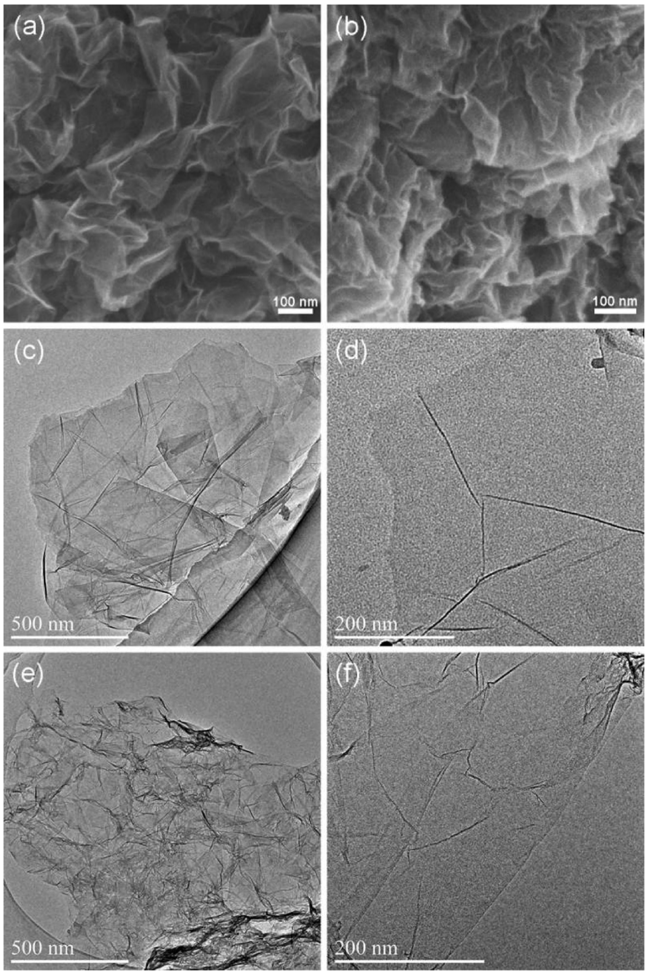

Figure 2. SEM images of (a) N-GO and (b) S-GO; TEM images of (c, d) N-CRG and (e, f) S-CRG.

than that of N-GO (0.717 nm). This is attributed to the fact that the deeply oxidized GO particles contain many more hydroxyl groups on the basal plane of graphene. After reduction, the XRD patterns of both N-CRG and S-CRG exhibit very weak diffraction peaks, due to the dissociation of long-range ordered stacking of GO by random interlayer exfoliation.[29] The nearly overlapped XRD patterns (Figure 3b) indicate almost the same crystalline structure for the two kinds of CRG.

The N_2 adsorption−desorption isotherms are employed to evaluate the difference of pore structure between N- and S-CRG. As shown in Figure 3c, both sorption isotherms exhibit the typical type IV isotherm with apparent H2 hysteresis loop according to IUPAC classification.[31] The specific BET surface area (S_{BET}), t-plot micropore surface area (<2 nm) (S_{micro}), total pore volume (V_P), and average pore size are shown in Table 1. It is noteworthy that the S_{BET} is tremendously increased from 468.2 m^2/g for N-CRG to 716.3 m^2/g for S-CRG. The great difference in S_{BET} is closely related to the average pore size and total pore volume. As presented in Figure 3d, the BJH adsorption pore size distribution shows that the pores in CRG are mainly meso- and macropores. Herein, according to Figure 3d, the average pore size of S-CRG is larger than that of N-CRG. The graphene sheets of S-CRG are more crimped to form smaller pores than that of N-CRG due to solvation. The pore volume (V_P) of CRG is up to 0.916 and 0.861 cm^3 g^{-1} for S-CRG and N-CRG, respectively, which is close to most of the ordered porous carbon materials (usually less than 1 cm^3 g^{-1}) .[32]

The nature of disorder in CRG is further investigated by Raman spectroscopy (Figure 3e). The peak positions and I_D/I_G ratios are listed in Table 1. As shown in Table 1, the I_D/I_G ratio of S-CRG (1.51) is relatively higher than that of N-CRG (1.27), which indicates that the crystallite size of S-CRG is small than that of N-CRG. This is closely related to the structural and elemental difference between N-CRG and S-CRG. On one hand, the decrease of lateral size introduces more edge sites; on the other hand, according to Table 2, the S-CRG has more oxygenic functional groups.

FT-IR spectrum was employed to identify the surface functional groups of CRG. As shown in Figure 3f, GO shows a wide hydroxyl stretch vibration mode of carboxyl, phenol, and/or intercalated H_2O (ν(O−H)) at 3410 cm^{-1}, and the C=O stretching vibration from carbonyl and carboxyl groups (ν(C=O)) at 1720 cm^{-1}. The adsorption peak at 1620 cm^{-1} is assigned to the components from the skeletal vibrations of unoxidized graphitic domains (δ(C=C)), while peaks at 1380, 1238, and 1076 cm^{-1} are attributed to the carboxyl C−O deformation vibrations (δ(O−H)), epoxy and/or ether type C−O−C (ν(C−O−C)), and alkoxy C−O stretching vibrations (ν(C−O)), respectively. After reduction, the peaks at 3410, 1620, 1380, and 1076 cm^{-1} are respectively blue-shifted to 3440, 1645, 1406, 1091 cm^{-1} with a remarkable lower intensity, while the peak at 1720 cm^{-1} nearly disappears.

Elemental analysis was adopted to characterize the components of the materials. As shown in Table 2, the oxygen content of S-GO (50.4%) is higher than that of N-GO (46.9%), which indicates a higher oxidization degree of S-GO. Compared with N-GO, the graphitic skeleton of graphene is more seriously destroyed in S-GO as more oxygenic functional groups, dangling bonds, and lattice defects are introduced. After reduction by hydrazine hydrate, oxygenic functionalities are partially removed. The oxygen content of S-CRG is still higher than that of N-CRG.

XPS analysis was employed to obtain the relative abundance of each oxygen and nitrogen containing functional groups on the surface of GO and CRG. The atomic percentages of C, O, and N heteroatoms, as well as the C/O atomic ratio are calculated and summarized in Table 2. The oxygen content of N-GO, S-GO, N-CRG, and S-CRG is 28.4, 31.1, 8.2, and 9.4 atom %, while the nitrogen content of N-CRG and S-CRG is 4.5 and 4.6 atom %, respectively, which is in accordance with the elemental analysis. As shown in Figure 4a−c, various C (C1−C5) and O (O1−O6) components in N-GO, S-GO, N-CRG, and S-CRG and N (N1−N5) components in N-CRG and S-CRG are further determined by fitting the C1s, O1s, and N1s fine scan spectra. The summaries of XPS fitting results, which quantitate the relative abundance of each species, are listed in Tables 3−5.

As shown in Table 3, the amount of C−C components in the materials is significantly increased after reduction (from 30.71 (N-GO) to 52.82 atom % (N-CRG) and 28.64 (S-GO) to 49.80 atom % (S-CRG)). As presented in Table 2, both the oxygen and nitrogen contents of S-CRG are higher than that of N-CRG. It is noteworthy that the abundance of quinone-type oxygen in S-CRG (2.06 atom %) is ca. 1.6 times higher than that in N-CRG (0.78 atom %), and the hydroxyl in S-CRG (1.36 atom %) is ca.1.4 times higher than that in N-CRG (0.94 atom %). The contents of C(O)O and C−O groups for S-CRG

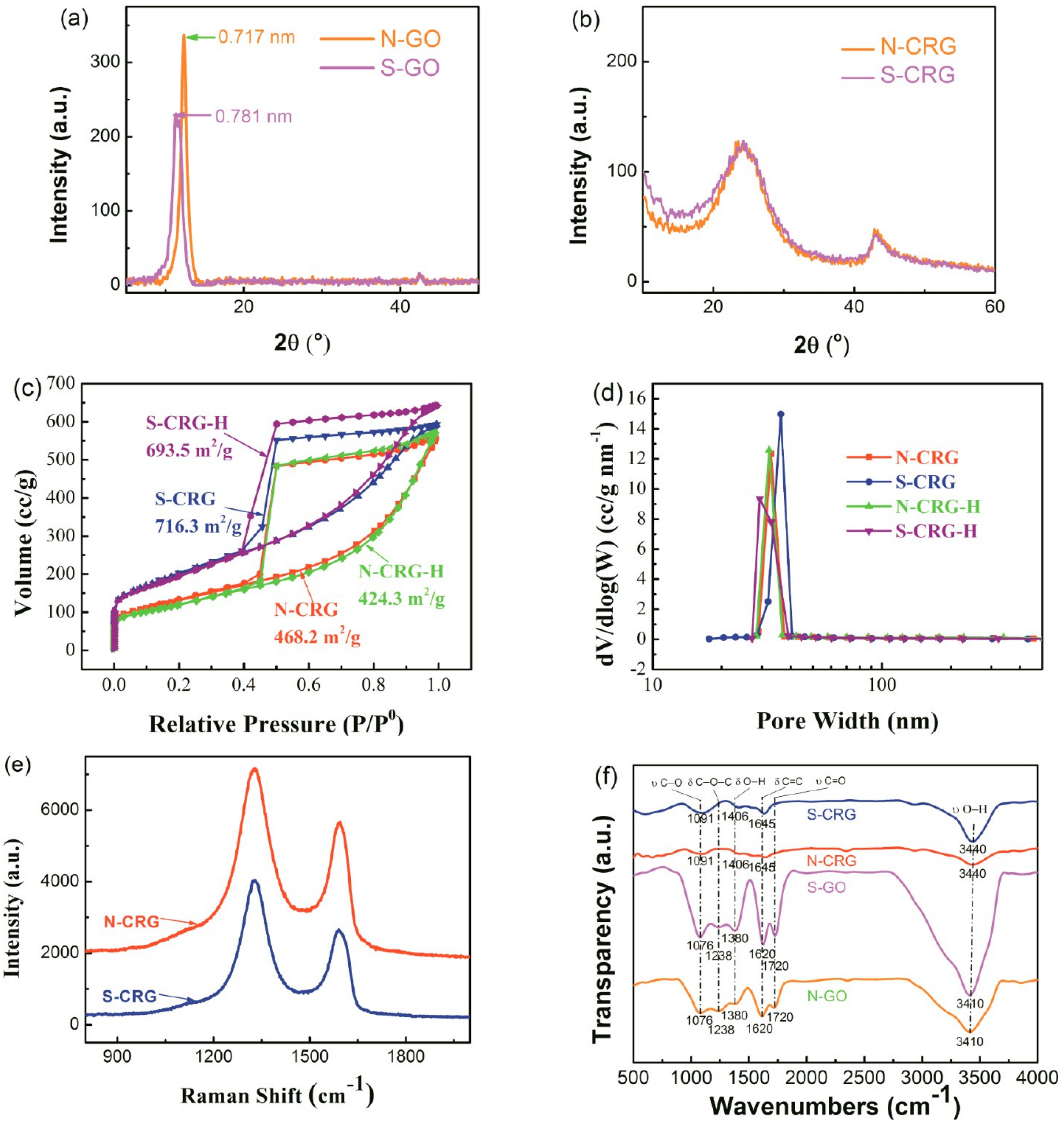

Figure 3. XRD patterns of (a) GO and (b) CRG; (c) N_2 physical adsorption isotherm of CRG; (d) BJH adsorption pore size distribution of CRG; (e) Raman spectrum of CRG; (f) FT-IR spectrum of CRG.

Table 1. Summary of Raman Result and Pore Structure of CRG

sample	D band[a] (cm^{-1})	G band[a] (cm^{-1})	I_D/I_G[a]	S_{BET}[b] (m^2 g^{-1})	S_{micro}[b] (m^2 g^{-1})	V_P[b] (mL g^{-1})
N-CRG	1329.2	1591.5	1.27	468.2	16.4	0.861
S-CRG	1327.2	1590.4	1.51	716.3	29.4	0.916

[a]Obtained from Raman spectra. [b]Calculated from N_2 physisorption isotherms.

are also higher than those of N-CRG. Besides, the amounts of amine/amide-type nitrogen for S-CRG (2.25 atom %) are ca. 20% higher than that of N-CRG (1.84 atom %). The electrochemical performance of CRGs is dependent on the abundance of quinone-type oxygen, hydroxyl, C(O)O, C−O, as well as amine/amide-type nitrogen functional groups..

The thermal stability of both GOs is characterized by TGA in Ar atmosphere. The retention of carbon atoms after thermal treatment is 52.5% (N-GO) and 45.0% (S-GO) (Figure 5). The order of thermal stability of various oxygen functional groups on carbon surface and corresponding gases released during the thermal decomposing is as follows: ether > carbonyl/quinones > epoxy > hydroxyl > carboxylic acids.[33−36] The deoxygenation and reduction process is simply divided into three stages: (I) the evaporation of physically adsorbed water from 30 to 150 °C;[33] (II) the release of CO_2, CO, and "chemical water" by evolution of surface functional groups from 150 to 300 °C; and (III) the steady carbonization with constant removal of oxygen from 300 to 1000 °C. It is noteworthy that the exothermic peak migrates from 217 °C for N-GO to 226 °C for S-GO.

3.2. Electrochemical Performance. The CRG-based supercapacitor electrodes were fabricated and characterized in a three-electrode system with 6.0 M KOH aqueous solution as the electrolyte. As revealed in Figure 6a, the CV curves for both CRG at a potential scan rate of 1.0 mV s^{-1} exhibit excellent capacitive behaviors, marked by the immediate current reverse upon reversal of the potential scan.[13] The capacitive current

Table 2. Elemental Composition of GO and CRG

sample	C^a (atom %)	O^a (atom %)	N^a (atom %)	C^b (wt %)	O^b (wt %)	N^a (wt %)	C/O atom ratio^a	residual C^c (%)
N-GO	70.0	28.4		49.5	46.9		2.47	52.4
S-GO	68.9	31.1		46.3	50.4		2.22	44.9
N-CRG	87.3	8.2	4.5	81.2	11.3	4.5	10.7	
S-CRG	86.0	9.4	4.6	74.5	16.3	6.2	9.1	

[a]Quantified by XPS analysis. [b]Obtained from elemental analysis. [c]Obtained from TGA (from room temperature to 1000 °C with rate of 10 deg/min in Ar).

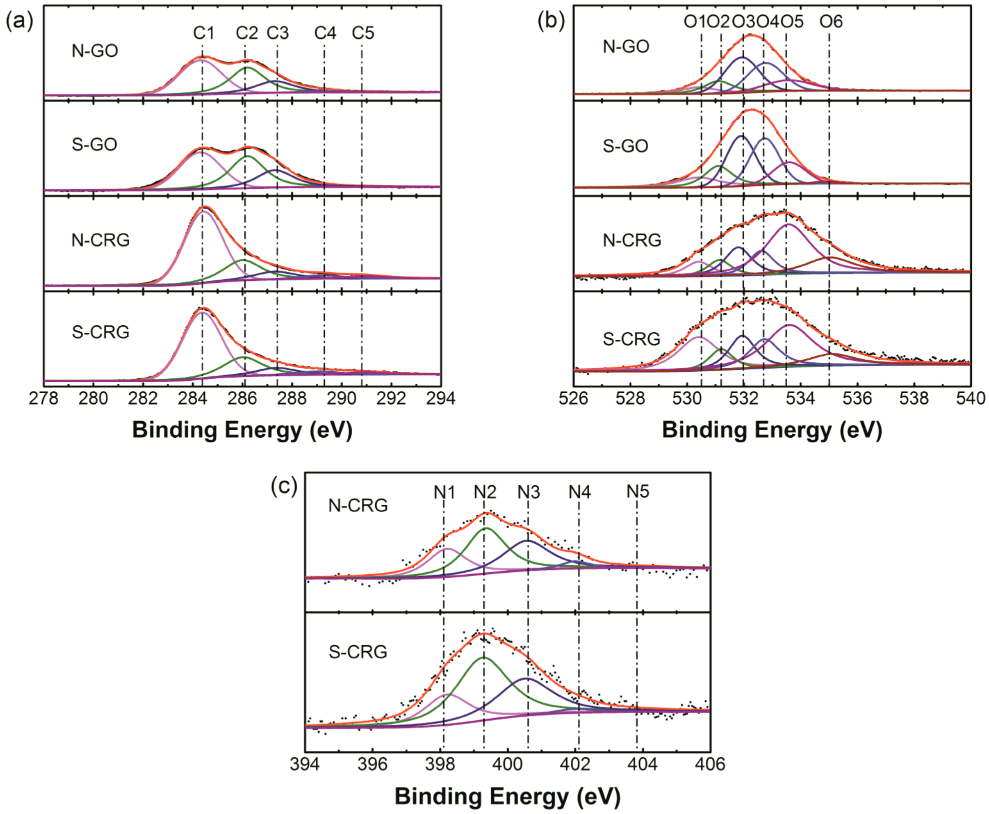

Figure 4. (a) The C1s and (b) O1s XPS fine scan spectra of N-GO, S-GO, N-CRG, and S-CRG; (c) N1s XPS fine scan spectrum of N-CRG and S-CRG.

Table 3. Fitted Results (atom %) of C1s XPS Spectra of GO and CRG

B.E. (eV)	C1 (284.4)	C2 (286.1)	C3 (287.4)	C4 (289.3)	C5 (290.8)
assignment	C−C	C−O	C=O	C(O)O	graphitic shakeup
N-GO	30.71	26.03	12.52	0.75	0.00
S-GO	28.64	26.55	13.76	0.00	0.00
N-CRG	52.82	19.38	8.37	3.84	2.82
S-CRG	49.80	20.49	7.96	4.23	3.49

Table 5. Fitted Results (atom %) of N1s XPS Spectra of CRG

B.E. (eV)	N1 (398.1)	N2 (399.3)	N3 (400.6)	N4 (402.1)	N5 (403.8)
assignment	pyridinic	amine/ amide	pyrrole/ pyridine	quaternary	*N*-oxide/ nitro
N-CRG	1.09	1.84	1.38	0.20	0.00
S-CRG	0.93	2.25	1.40	0.01	0.00

increases quickly from N-CRG to S-CRG, while the CV curve of S-CRG approaches a nearly rectangular shape.

Table 4. Fitted Results (atom %) of O1s XPS Spectra of GO and CRG

B.E. (eV)	O1 (530.5)	O2 (531.2)	O3 (531.9)	O4 (532.7)	O5 (533.5)	O6 (535)
assignment	quinone	C(O)O	C=O	C−O	O−H	H_2O
N-GO	2.38	3.80	9.72	8.25	4.20	0.00
S-GO	3.21	4.90	9.23	8.63	4.63	0.45
N-CRG	0.78	0.55	1.24	0.94	3.50	1.16
S-CRG	2.06	0.74	1.34	1.36	3.11	0.82

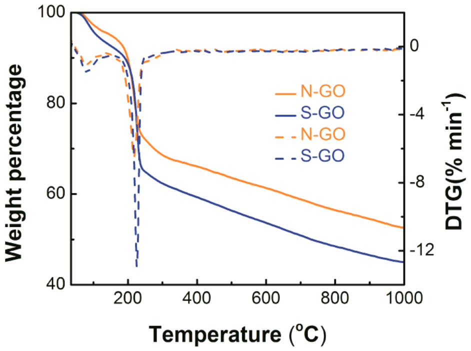

Figure 5. TG analysis of N-GO and S-GO.

The CV profiles at different scan rates from 1.0 to 200 mV s^{-1} are collected to evaluate the rapid charging/discharging abilities of both CRG samples. The specific capacitance values of all the CRGs calculated from CVs at different scan rates are shown in Figure 6b. Among the whole range of potential scan rates, the S-CRG exhibits higher capacitance than N-CRG. The initial capacitance of S-CRG and N-CRG at a slow scan rate of 1.0 mV s^{-1} reaches 192.1 (0.27 F m^{-2}) and 132.3 F g^{-1} (0.28 F m^{-2}). With the increase of scan rate, the EDLC becomes the primary electrochemical manner of electrodes due to the delay potential during reversing the potential sweep, which is connected with a kinetically slow process of PC involved during charging/discharging.[1]

To clarify the relative contribution of EDLC (C_{EDLC}) and PC (C_{PC}) to the total capacitance (C_{total}), the surface functional groups within N-CRG and S-CRG were further removed by carbonization at 1000 °C to obtain N-CRG-H and S-CRG-H. Thus, most of the C_{PC} from O and N heteroatoms can be excluded, and the capacitive value of CRG-H is roughly equal to the C_{EDLC} of CRG. As shown in Figure 6c, the C_{EDLC} of S-CRG and N-CRG at 1.0 mV s^{-1} is 63.3 and 36.8 F g^{-1}, respectively. Providing $C_{total} = C_{EDLC} + C_{PC}$, then the contribution of C_{PC} for S-CRG and N-CRG is calculated to be 128.8 and 95.5 F g^{-1}, which accounts for 67.0% and 72.2% of the C_{total}, respectively. It has been reported that mainly carbonyl/hydroxyl-type groups contribute to the PC, rather than the other oxygen-containing functional groups.[37−39] This is in accordance with the chemical analysis result (Table 2) that S-CRG owns much more functionalities than N-CRG, which provide more PC.[40,41]

Figure 7a shows the GC curves of both CRG at the current density of 0.5 A g^{-1}. The capacitance calculated from the discharge curves is 121.7 and 179.6 F g^{-1} for N-CRG and S-CRG, respectively. The EIS is introduced to examine the fundamental behavior of the electrode materials for supercapacitors in the frequency range from 200 kHz to 10 mHz yielding the Nyquist plot shown in Figure 7b. An equivalent circuit model (inset of Figure 7b) is employed to simulate the capacitive and resistive elements of the cells under analysis.[42] The intercept in the high-frequency region reflects the internal resistance of CRG-based electrode (R_i), while the radius of the semicircle impedance loop indicates the resistance due to contact interface (R_c). The 45° in the middle frequency range represents the Warburg resistance (Z_w), which is related to ion diffusion in the electrolyte. The slope of the line at low frequency range reflects the capacitance characteristics of the electrode materials. As shown in the insert of Figure 7b, the N-CRG ($R_i = 0.84\ \Omega$) exhibits a relatively lower internal resistance than that of S-CRG (0.93 Ω) due to the difference in oxygen content between N-CRG and S-CRG as indicated in elemental

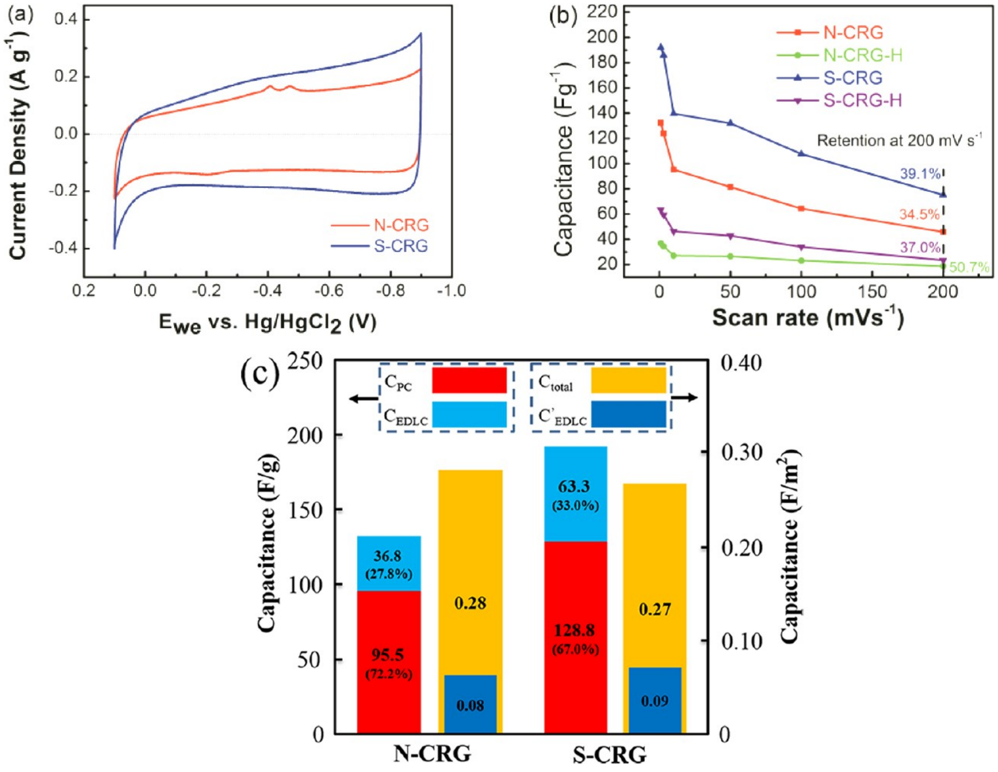

Figure 6. (a) CV profiles of N-CRG and S-CRG at 1.0 mV/s; (b) C_F versus scan rates for N-CRG and S-CRG; (c) the relative ratio of C_{EDLC} and C_{PC} for N-CRG and S-CRG.

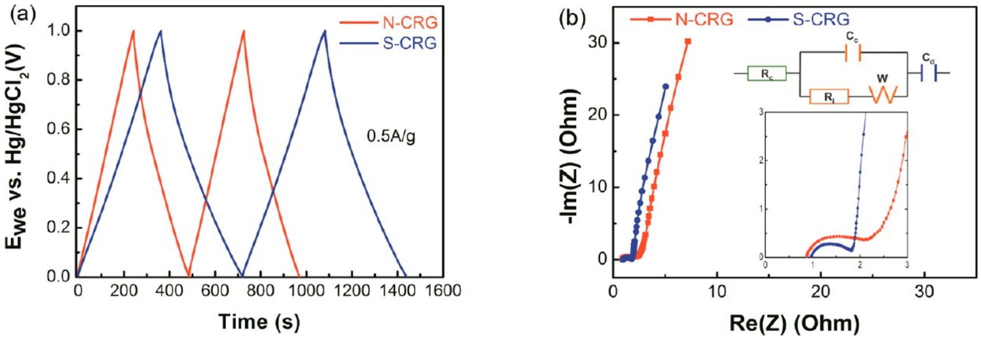

Figure 7. (a) The Galvanostatic charging/discharging curves and (b) The Nyquist plot of N-CRG and S-CRG; the inset shows the enlarged Nyquist plot and equivalent circuit model.

analysis.[43] Compared with N-CRG (R_c = 0.78 Ω), S-CRG (R_c = 0.48 Ω) has a much lower resistance in electrolyte transportation, demonstrating a shorter and smoother path for electron transportation and electrolyte penetration, as more oxygen containing functional groups in S-CRG could improve the surface wettability of the electrodes.[44] In addition, the straight line for S-CRG at low frequency range is much closer to 90° than N-CRG, indicating a better capacitive performance for S-CRG.

The reversible Faradic redox mechanism of O and N atoms in enhancing the capacitance in the electrolyte has been widely investigated.[35,45] The basal plane of CRG sheet is composed of abundant sp^2 graphitic domains and distorted sp^3 carbons decorated by various oxygenous and nitrous functional groups. The inductive effects aroused from the O and N atoms cause the polarization of some bonds. Consequently, the reversible redox reactions are likely to take place on the polarized sites during the charging/discharging process. In addition, the basic functional groups such as quinone and amine groups may play the key role in enhancing the PC. Figure 8 shows the influence of structural difference between N-CRG and S-CRG on capacitive charging. Obviously, S-CRG has more edge sites than N-CRG with the same area. This provides the chance for introducing more quinone and amine-type groups as demonstrated in XPS results.

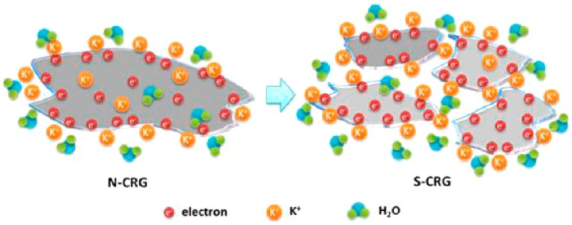

Figure 8. Schematic illustration of the difference in capacitive charging for N-CRG and S-CRG.

The cycling stability tests were carried out by repeating charging/discharging process at a scan rate of 50 mV s^{-1}. As shown in Figure 9, after 3000 times of cycling, the specific capacitance of S-CRG was reduced to 97.3% of the first cycle, while N-CRG still holds a capacitive retention of as high as 98.5%. The different cycling life of both CRGs is due to the difference in surface functional groups. The abundant O and N heteroatoms, which contribute more PC-active sites for charge storage in S-CRG, may also bring down the electrochemical stability of the electrode, as more unstable groups are likely to be eliminated during the repeating charging/discharging process.[46,47]

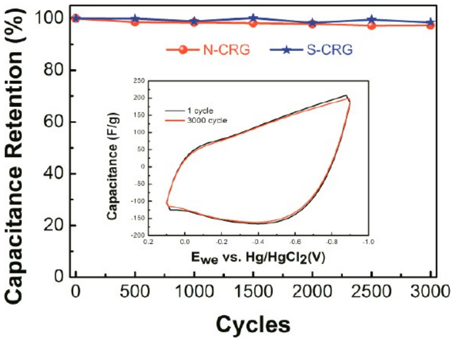

Figure 9. Cycling performance of both CRGs. The inset shows the first and 3000th cycle CV profiles of S-CRG at a scan rate of 50 mV s^{-1} in 6.0 M KOH.

4. CONCLUSIONS

The CRGs with unique microtexture, pore structure, surface chemistry, and good electrochemical performance were prepared by the reduction of GO in different oxidation degrees. Compared to N-GO and N-CRG, the S-GO and S-CRG have higher oxygen content and more oxygenic functional groups that contribute to the PC. Meanwhile, the relatively smaller average pore size results in higher specific surface area which is responsible to the EDLC. Compared with N-CRG, the S-CRG exhibits higher specific capacitance (enhanced from 132.3 to 192.1 F g^{-1}) and performs better capacitance characteristics while the cycle life has a slight decrease (from 98.5 to 97.3% after 3000 times cycling). These results shed a new light not only on the mechanistic understanding of the structure, property, and capacitive performance of graphene, but also on the manipulating strategy for pristine graphene-based electrodes with improved properties for advanced energy storage.

■ ASSOCIATED CONTENT

Ⓢ Supporting Information

Details of preparation of graphite oxide. This material is available free of charge via the Internet at http://pubs.acs.org.

■ AUTHOR INFORMATION

Corresponding Author

*E-mail: ccm@sxicc.ac.cn. Fax: 86-351-4049061.

Notes

Notes. The authors declare no competing financial interest.

■ ACKNOWLEDGMENTS

The author would like to acknowledge the financial support from the Innovative Research Fund of ICC-CAS (2012SCXQT03), the Natural Science Foundation of Shanxi Province (2013011012-7), the Innovative Research Fund of Taiyuan Science and Technology Bureau (2012CXJD0510), Shanxi Coal Transportation and Sales Group Co. Ltd. (2013WT103) and Research Fund for the Doctoral Program of Higher Education of China (20120002120047).

■ REFERENCES

(1) Frackowiak, E.; Beguin, F. Carbon Materials for the Electrochemical Storage of Energy in Capacitors. *Carbon* **2001**, *39*, 937−950.

(2) Simon, P.; Gogotsi, Y. Materials for Electrochemical Capacitors. *Nat. Mater.* **2008**, *7*, 845−854.

(3) Su, D. S.; Schlogl, R. Nanostructured Carbon and Carbon Nanocomposites for Electrochemical Energy Storage Applications. *ChemSusChem* **2010**, *3*, 136−168.

(4) Inagaki, M.; Konno, H.; Tanaike, O. Carbon Materials for Electrochemical Capacitors. *J. Power Sources* **2010**, *195*, 7880−7903.

(5) Zhu, Y. W.; Murali, S.; Stoller, M. D.; Ganesh, K. J.; Cai, W. W.; Ferreira, P. J.; Pirkle, A.; Wallace, R. M.; Cychosz, K. A.; Thommes, M.; et al. Carbon-Based Supercapacitors Produced by Activation of Graphene. *Science* **2011**, *332*, 1537−1541.

(6) Su, F. Y.; You, C. H.; He, Y. B.; Lv, W.; Cui, W.; Jin, F. M.; Li, B. H.; Yang, Q. H.; Kang, F. Y. Flexible and Planar Graphene Conductive Additives for Lithium-Ion Batteries. *J. Mater. Chem.* **2010**, *20*, 9644−9650.

(7) Zhao, M. Q.; Zhang, Q.; Huang, J. Q.; Tian, G. L.; Chen, T. C.; Qian, W. Z.; Wei, F. Towards High Purity Graphene/Single-Walled Carbon Nanotube Hybrids with Improved Electrochemical Capacitive Performance. *Carbon* **2013**, *54*, 403−411.

(8) Stoller, M. D.; Park, S. J.; Zhu, Y. W.; An, J. H.; Ruoff, R. S. Graphene-Based Ultracapacitors. *Nano Lett.* **2008**, *8*, 3498−3502.

(9) Lv, W.; Tang, D. M.; He, Y. B.; You, C. H.; Shi, Z. Q.; Chen, X. C.; Chen, C. M.; Hou, P. X.; Liu, C.; Yang, Q. H. Low-Temperature Exfoliated Graphenes: Vacuum-Promoted Exfoliation and Electrochemical Energy Storage. *ACS Nano* **2009**, *3*, 3730−3736.

(10) Wang, Y.; Shi, Z. Q.; Huang, Y.; Ma, Y. F.; Wang, C. Y.; Chen, M. M.; Chen, Y. S. Supercapacitor Devices Based on Graphene Materials. *J. Phys. Chem. C* **2009**, *113*, 13103−13107.

(11) Vivekchand, S. R. C.; Rout, C. S.; Subrahmanyam, K. S.; Govindaraj, A.; Rao, C. N. R. Graphene-Based Electrochemical Supercapacitors. *J. Chem. Sci.* **2008**, *120*, 9−13.

(12) Yang, X. W.; Zhu, J. W.; Qiu, L.; Li, D. Bioinspired Effective Prevention of Restacking in Multilayered Graphene Films: Towards the Next Generation of High-Performance Supercapacitors. *Adv. Mater.* **2011**, *23*, 2833−2838.

(13) El-Kady, M. F.; Strong, V.; Dubin, S.; Kaner, R. B. Laser Scribing of High-Performance and Flexible Graphene-Based Electrochemical Capacitors. *Science* **2012**, *335*, 1326−1330.

(14) Niu, Z. Q.; Chen, J.; Hng, H. H.; Ma, J.; Chen, X. D. A Leavening Strategy to Prepare Reduced Graphene Oxide Foams. *Adv. Mater.* **2012**, *24*, 4144−4150.

(15) Li, F. H.; Song, J. F.; Yang, H. F.; Gan, S. Y.; Zhang, Q. X.; Han, D. X.; Ivaska, A.; Niu, L. One-Step Synthesis of Graphene/SnO_2 Nanocomposites and Its Application in Electrochemical Supercapacitors. *Nanotechnology* **2009**, *20*, 455−602.

(16) Cao, X. H.; Shi, Y. M.; Shi, W. H.; Lu, G.; Huang, X.; Yan, Q. Y.; Zhang, Q. C.; Zhang, H. Preparation of Novel 3D Graphene Networks for Supercapacitor Applications. *Small* **2011**, *7*, 3163−3168.

(17) Yan, J.; Wei, T.; Qiao, W. M.; Shao, B.; Zhao, Q. K.; Zhang, L. J.; Fan, Z. J. Rapid Microwave-Assisted Synthesis of Graphene Nanosheet/Co_3O_4 Composite for Supercapacitors. *Electrochim. Acta* **2010**, *55*, 6973−6978.

(18) Huang, Y.; Liang, J. J.; Chen, Y. S. An Overview of the Applications of Graphene-Based Materials in Supercapacitors. *Small* **2012**, *8*, 1805−1834.

(19) Chen, S.; Xing, W.; Duan, J. J.; Hu, X. J.; Qiao, S. Z. Nanostructured Morphology Control for Efficient Supercapacitor Electrodes. *J. Mater. Chem. A* **2013**, *1*, 2941−2954.

(20) Fan, Z. J.; Yan, J.; Zhi, L. J.; Zhang, Q.; Wei, T.; Feng, J.; Zhang, M. L.; Qian, W. Z.; Wei, F. A Three-Dimensional Carbon Nanotube/Graphene Sandwich and Its Application as Electrode in Supercapacitors. *Adv. Mater.* **2010**, *22*, 3723−3728.

(21) Pumera, M. Graphene-Based Nanomaterials and Their Electrochemistry. *Chem. Soc. Rev.* **2010**, *39*, 4146−4157.

(22) Sun, Y. Q.; Wu, Q. O.; Shi, G. Q. Graphene Based New Energy Materials. *Energy Environ. Sci.* **2011**, *4*, 1113−1132.

(23) Pei, S. F.; Cheng, H. M. The Reduction of Graphene Oxide. *Carbon* **2012**, *50*, 3210−3228.

(24) Zhang, L.; Liang, J.; Huang, Y.; Ma, Y.; Wang, Y.; Chen, Y. Size-Controlled Synthesis of Graphene Oxide Sheets on a Large Scale Using Chemical Exfoliation. *Carbon* **2009**, *47*, 3365−3380.

(25) Chen, C. M.; Yang, Q. H.; Yang, Y. G.; Lv, W.; Wen, Y. F.; Hou, P. X.; Wang, M. Z.; Cheng, H. M. Self-Assembled Free-Standing Graphite Oxide Membrane. *Adv. Mater.* **2009**, *21*, 3007−3011.

(26) Park, S.; An, J.; Potts, J. R.; Velamakanni, A.; Murali, S.; Ruoff, R. S. Hydrazine-Reduction of Graphite- and Graphene Oxide. *Carbon* **2011**, *49*, 3019−3023.

(27) Jung, I.; Vaupel, M.; Pelton, M.; Piner, R.; Dikin, D. A.; Stankovich, S.; An, J.; Ruoff, R. S. Characterization of Thermally Reduced Graphene Oxide by Imaging Ellipsometry. *J. Phys. Chem. C* **2008**, *112*, 8499−8506.

(28) Ni, Z. H.; Wang, H. M.; Kasim, J.; Fan, H. M.; Yu, T.; Wu, Y. H.; Feng, Y. P.; Shen, Z. X. Graphene Thickness Determination Using Reflection and Contrast Spectroscopy. *Nano Lett.* **2007**, *7*, 2758−2763.

(29) Schniepp, H. C.; Li, J. L.; McAllister, M. J.; Sai, H.; Herrera-Alonso, M.; Adamson, D. H.; Prud'homme, R. K.; Car, R.; Saville, D. A.; Aksay, I. A. Functionalized Single Graphene Sheets Derived from Splitting Graphite Oxide. *J. Phys. Chem. B* **2006**, *110*, 8535−8539.

(30) Meyer, J. C.; Geim, A. K.; Katsnelson, M. I.; Novoselov, K. S.; Booth, T. J.; Roth, S. The Structure of Suspended Graphene Sheets. *Nature* **2007**, *446*, 60−63.

(31) Chen, C. M.; Zhang, Q.; Huang, J. Q.; Zhang, W.; Zhao, X. C.; Huang, C. H.; Wei, F.; Yang, Y. G.; Wang, M. Z.; Su, D. S. Chemically Derived Graphene-Metal Oxide Hybrids as Electrodes for Electrochemical Energy Storage: Pre-Graphenization or Post-Graphenization? *J. Mater. Chem.* **2012**, *22*, 13947−13955.

(32) Vix-Guterl, C.; Frackowiak, E.; Jurewicz, K.; Friebe, M.; Parmentier, J.; Beguin, F. Electrochemical Energy Storage in Ordered Porous Carbon Materials. *Carbon* **2005**, *43*, 1293−1302.

(33) Bagri, A.; Mattevi, C.; Acik, M.; Chabal, Y. J.; Chhowalla, M.; Shenoy, V. B. Structural Evolution During the Reduction of Chemically Derived Graphene Oxide. *Nat. Chem.* **2010**, *2*, 581−587.

(34) Chen, C. M.; Huang, J. Q.; Zhang, Q.; Gong, W. Z.; Yang, Q. H.; Wang, M. Z.; Yang, Y. G. Annealing a Graphene Oxide Film to Produce a Free Standing High Conductive Graphene Film. *Carbon* **2012**, *50*, 659−667.

(35) Chen, C. M.; Zhang, Q.; Yang, M. G.; Huang, C. H.; Yang, Y. G.; Wang, M. Z. Structural Evolution During Annealing of Thermally Reduced Graphene Nanosheets for Application in Supercapacitors. *Carbon* **2012**, *50*, 3572−3584.

(36) Figueiredo, J. L.; Pereira, M. F. R. The Role of Surface Chemistry in Catalysis with Carbons. *Catal. Today* **2010**, *150*, 2−7.

(37) Liu, C. G.; Yu, Z. N.; Neff, D.; Zhamu, A.; Jang, B. Z. Graphene-Based Supercapacitor with an Ultrahigh Energy Density. *Nano Lett.* **2010**, *10*, 4863−4868.

(38) Lin, Z. Y.; Liu, Y.; Yao, Y. G.; Hildreth, O. J.; Li, Z.; Moon, K.; Wong, C. P. Superior Capacitance of Functionalized Graphene. *J. Phys. Chem. C* **2011**, *115*, 7120−7125.

(39) Salgado, S.; Pu, L.; Maheshwari, V. Targeting Chemical Morphology of Graphene Oxide for Self-Assembly and Subsequent Templating of Nanoparticles: A Composite Approaching Capacitance Limits in Graphene. *J. Phys. Chem. C* **2012**, *116*, 12124−12130.

(40) Wang, Y. G.; Li, H. Q.; Xia, Y. Y. Ordered Whiskerlike Polyaniline Grown on the Surface of Mesoporous Carbon and Its Electrochemical Capacitance Performance. *Adv. Mater.* **2006**, *18*, 2619−2623.

(41) Xu, G. H.; Zheng, C.; Zhang, Q.; Huang, J. Q.; Zhao, M. Q.; Nie, J. Q.; Wang, X. H.; Wei, F. Binder-Free Activated Carbon/Carbon Nanotube Paper Electrodes for Use in Supercapacitors. *Nano Res.* **2011**, *4*, 870−881.

(42) Chen, C. M.; Zhang, Q.; Huang, C. H.; Zhao, X. C.; Zhang, B. S.; Kong, Q. Q.; Wang, M. Z.; Yang, Y. G.; Cai, R.; Su, D. S. Macroporous 'Bubble' Graphene Film via Template-Directed Ordered-Assembly for High Rate Supercapacitors. *Chem. Commun.* **2012**, *48*, 7149−7151.

(43) Jung, I.; Dikin, D. A.; Piner, R. D.; Ruoff, R. S. Tunable Electrical Conductivity of Individual Graphene Oxide Sheets Reduced at "Low" Temperatures. *Nano Lett.* **2008**, *8*, 4283−4287.

(44) Lee, S. H.; Kim, H. W.; Hwang, J. O.; Lee, W. J.; Kwon, J.; Bielawski, C. W.; Ruoff, R. S.; Kim, S. O. Three-Dimensional Self-Assembly of Graphene Oxide Platelets into Mechanically Flexible Macroporous Carbon Films. *Angew. Chem., Int. Ed.* **2010**, *49*, 10084−10088.

(45) Chen, C. M.; Zhang, Q.; Zhao, X. C.; Zhang, B. S.; Kong, Q. Q.; Yang, M. G.; Yang, Q. H.; Wang, M. Z.; Yang, Y. G.; Schlogl, R.; et al. Hierarchically Aminated Graphene Honeycombs for Electrochemical Capacitive Energy Storage. *J. Mater. Chem.* **2012**, *22*, 14076−14084.

(46) Choi, N.-S.; Chen, Z.; Freunberger, S. A.; Ji, X.; Sun, Y.-K.; Amine, K.; Yunshin, G.; Nazar, L. F.; Cho, J.; Bruce, P. G. Challenges Facing Lithium Batteries and Electrical Double-Layer Capacitors. *Angew. Chem., Int. Ed.* **2012**, *51*, 2−33.

(47) Pandolfo, A. G.; Hollenkamp, A. F. Carbon Properties and Their Role in Supercapacitors. *J. Power Sources* **2006**, *157*, 11−27.